Progress in Natural Science: Materials International 36 (2026) 52–64

HOSTED BY

Contents lists available at ScienceDirect

Progress in Natural Science: Materials International

journal homepage: www.elsevier.com/locate/pnsmi

Facile preparation of $Ni_xCo_{1-x}(OH)_2$/N-doped porous carbon nanocomposites with superior electrochemical performances for hybrid supercapacitors

Yulai Zhao[a,b], Yuxuan Chen[a], Haoran Chen[a], Longqiang Xiao[a,b], Xuehui Ge[a,*], Xiangyu Yin[a], Linxi Hou[a,b,**]

[a] Department of Materials-Oriented Chemical Engineering, College of Chemical Engineering, Fuzhou University, Fuzhou, 350116, China
[b] Qingyuan Innovation Laboratory, Quanzhou, 362801, China

ARTICLE INFO

Keywords:
Ni/Co hydroxide
High internal phase emulsion templating
N-doped porous carbon
Hybrid supercapacitor
Nanocomposites

ABSTRACT

The urgent need for high-performance energy storage devices has been driving the quest for superior battery-type electrode materials for hybrid supercapacitors (HSCs), however the relevant synthesis methods are usually tedious and poorly affordable. In this paper, a two-step route was elaborated to prepare Ni,Co hydroxide/N-doped porous carbon ($Ni_xCo_{1-x}(OH)_2$/NPC) nanocomposites for hybrid supercapacitors. NPC with unique three-dimensional interconnected porous structure was obtained by HIPE high internal phase emulsion (HIPE) polymerization with subsequent pyrolysis. The NPC can act not only as a conductive network providing abundant accessible area and convenient charge transfer routes, but also as an anchoring platform for $Ni_xCo_{1-x}(OH)_2$ growth via chemical bath deposition (CBD) without agglomeration. By tuning Ni^{2+}/Co^{2+} ratio, the optimized $Ni_xCo_{1-x}(OH)_2$/NPC nanocomposite exhibited excellent electrochemical performance with a capacity of 1392 F g^{-1} at 1 A g^{-1} in 6 M KOH solution. Furthermore, coupling with an activated NPC anode, the assembled hybrid supercapacitor possessed an appreciable energy density of 118.9 Wh kg^{-1} at 400.0 W kg^{-1} and a capacitance retention ratio of 80.7 % after 5000 charge-discharge cycles, showing considerable application prospects. This work provides new inspirations for the reasonable design and optimization of new electrode materials for first-rate hybrid supercapacitors.

1. Introduction

Rapid industrialization, climate change and the depletion of non-renewable fossil fuel resources (e.g., coal, oil, and natural gas) demand researchers and industry to embrace sustainable and renewable energy sources, such as solar energy, wind energy, tidal energy, etc [1, 2]. However, the commercialization of renewable energy sources is still a significant challenge, as their intermittent peculiarity limits them to generate electricity power steadily. As a result, efficient energy storage systems acting as buffer guarantee are essential for the secure and continuous power supply [3,4]. Among various energy storage technologies, supercapacitors are considered to be one of the most promising candidates for energy storage since they have significant advantages in terms of high power density, fast charging rate, long cycle life, low cost, and environmental friendliness, which enable them to be used as an important supplement to batteries in the applications requiring rapid energy transfer and high power density, thus attracting considerable attentions from researchers and industry [4–6].

Although supercapacitors have been widely used for auxiliary applications such as peak power compensation and starter power, the bottleneck of limited energy density resulted from narrow voltage window and/or low specific capacitance, prevents their wider application as primary power sources [7–9]. Aqueous electrolytes are favored because of their low cost, high safety, and low internal resistance. However, the maximum operating voltage for aqueous electrolyte based symmetric supercapacitors is usually around 1.0 V [4,6], determined by the stable potential cap of water (1.23 V) [6,10]. There are two ways to improve the energy density: 1) to increase the specific capacitance of the whole supercapacitor, which depends on further development of novel electrode materials; 2) to increase the voltage range for supercapacitor operation.

* Corresponding author.
** Corresponding author. Department of Materials-Oriented Chemical Engineering, College of Chemical Engineering, Fuzhou University, Fuzhou, 350116, China.
E-mail addresses: gexuehui@fzu.edu.cn (X. Ge), lxhou@fzu.edu.cn (L. Hou).

https://doi.org/10.1016/j.pnsc.2025.06.003
Received 19 March 2025; Received in revised form 4 June 2025; Accepted 5 June 2025
Available online 4 February 2026

An effective strategy to obtain high energy density of supercapacitors is to assemble a hybrid supercapacitor (HSC) consisting of a battery-type electrode and a capacitor-type electrode [10–12]. HSC can take full advantage of the different voltage windows of the two types of electrodes by the compensating effect of reverse overpotential since the battery-type and capacitor-type electrodes possess the positive and negative voltage windows, respectively [10]. In addition to the proper matching of the positive and negative electrodes, the electrochemical properties of HSC are closely related to the performance of the battery-type electrodes, which is determined by their chemical composition and porous structure [12,13].

Transition metal-based materials (TMMs) are particularly attractive because of their abundant redox reactions, high specific capacitance, low cost, diverse chemical compositions, easy preparation, etc [4,14,15]. However, there are several defects such as low conductivity, low material utilization degree, poor cycling stability and rate performances [16–18]. One solution to the problems is to develop composite materials consisting of two or more types of TMMs which not only facilitate the increase of the overall specific capacitance, but also improve the strength [19–25]. For example, Mohapatra et al. [26] explored the synergistic effect of the metal oxides in MoO_3@Co_3O_4 nanocomposites and found that the introduction of MoO_3 increased the specific capacitance from 1027 F g^{-1} to 1248 F g^{-1}. Xiao et al. [7] designed a layered hybrid electrode by integrating nano-needle structured $NiCo_2O_4$ and Ni, Mn layered double hydroxide (NiMn-LDH) composites on highly conductive carbon cloth. The electrode retains the high specific capacitance of NiMn-LDH and combines the high rate performance of $NiCo_2O_4$, with a specific capacitance of 932.6 F g^{-1} at 1 mA cm^{-2} and a rate performance of 59.8 % at 50 mA cm^{-2}.

To overcome the problems of volume expansion, low conductivity, and liable aggregation of nanoscale TMMs, constructing carbon-supported/enfolded nanoscale TMMs is another reliable solution [2,27,28]. Commonly used carbon substrates are graphene [29,30], carbon nanotubes [31,32], and carbon dots [11,27], which are difficult to prepare and costly, severely limiting the large-scale application of such materials [33,34]. Porous carbons, especially N-doped porous carbons (NPCs) possess abundant porous structures which can increase the capacitance value and contribute to the charge diffusion during the charging/discharging process, thus improving electrode energy density and cycling stability. Among various preparation methods, high internal phase emulsion (HIPE) template is an effective method to prepare porous polymers (polyHIPEs) with unique and controllable porous structure, as well as high porosity [35]. Three-dimensional (3D) interconnected porous carbon materials can be obtained from polyHIPEs via high temperature pyrolysis. The obtained freestanding, conductive porous carbon frameworks with highly controllable porous structure are promising backbone of energy storage devices to effectively anchor transition metal hydroxides to avoid agglomeration or restacking [36,37].

It has been the case that α-$Ni(OH)_2$ has been attracting wide research attentions as a battery-type electrode with an ultra-high theoretical capacitance of 2365 F g^{-1}, which is more considerable than NiO and NiS_x [30,38]. The introduction of cobalt in $Ni(OH)_2$ can effectively reduce the band gap and induce electron conduction and excitation, while preventing irreversible phase changes during cycling and enhancing the structural stability of electrode materials. Chemical bath deposition (CBD) is a simple, efficient, green and economical synthesis method with merits of milder reaction conditions, less energy and time consumption than hydrothermal methods [39,40]. Also the chemical composition of the product is highly adjustable [1].

Herein, we report a route to prepare Ni,Co hydroxide/N-doped porous carbon ($Ni_xCo_{1-x}(OH)_2$/NPC) composites as superior battery-type electrode materials for hybrid supercapacitors via HIPE template method with subsequent CBD. NPC with 3D interconnected porous structures was derived from polyHIPE. Then $Ni_xCo_{1-x}(OH)_2$ with different compositions were loaded onto the NPC substrate by CBD. By tuning the Ni^{2+}/Co^{2+} ratio, the optimized $Ni_xCo_{1-x}(OH)_2$/NPC sample reaches to a high capacitance of 1392 F g^{-1} at 1 A g^{-1}. Furthermore, with activated NPC (ANPC) as anode, the assembled $Ni_xCo_{1-x}(OH)_2$/NPC//ANPC HSC possesses an appreciable energy density of 118.9 Wh kg^{-1} at 400.0 W kg^{-1}, showing considerable application promise.

2. Experimental section

2.1. Chemicals and materials

Tween 20, resorcinol, melamine, formaldehyde aqueous solution (37 wt%), ethanol, polytetrafluoroethylene (PTFE), potassium hydroxide (KOH), urea, and sodium carbonate (Na_2CO_3) were purchased from Shanghai Aladdin Biochemical Technology Co., Ltd. Nickel acetate tetrahydrate ($(CH_3COO)_2Ni{\cdot}4H_2O$) and cobalt acetate ($(CH_3COO)_2Co$) were purchased from Shanghai Macklin Biochemical Co., Ltd. Hydrochloric acid (HCl) and xylene were obtained from Sinopharm Chemical Reagent Co., Ltd. Acetylene black was supplied by KJ Group, MTI Corporation. Deionized water was used in the work thoroughly. Unless otherwise stated, all chemicals are analytically pure and used without further purification.

2.2. Synthesis of NPCs

As we reported previously, NPC was synthesized based on HIPE templating method [41]. Specifically, 0.01 mol of resorcinol, 0.015 mol of melamine and 0.005 g of Na_2CO_3 (to adjust the solution pH to 9.0) were dispersed in excess formaldehyde (5 mL, 0.067 mol) with 0.2 mL deionized water. The above suspension was heated in a water bath at 60 °C for 5 min until clarified, which was then cooled with ice water to obtain a prepolymer solution.

Emulsifier Tween 20 (1.0 g) was added to the prepolymer solution, then 30 mL of xylene was added dropwise to the aqueous phase as the internal phase under mechanical stirring at 550 rpm for about 30 min, stirring for another 90 min. 0.5 mL of HCl solution (1 mol L^{-1}) was added dropwise to the formed emulsion and stirred 3 min. After sealing, the HIPE was polymerized at 70 °C for 24 h to provide crude polyHIPE which was soxhlet extracted with ethanol for 24 h to remove xylene. After drying, the prepared polyHIPE was pyrolyzed under nitrogen protection at 700 °C for 2 h with a heating rate of 2 °C min^{-1} to obtain NPCs.

2.3. Synthesis of $Ni_xCo_{1-x}(OH)_2$/NPCs

The NPCs prepared as above were immersed in mixed acid (1:1 vol ratio of sulfuric acid and nitric acid) for 24 h, and washed until the pH of the leachate was 7. Then 0.07 g of dry NPCs were added to 30 mL of deionized water dissolved with nickel acetate, cobalt acetate, and urea (32 mmol). After vacuum immersed for 24 h, the reaction was carried out in a water bath of 90 °C for 2 h (where the total amount of nickel acetate and cobalt acetate was 8 mmol with the Ni^{2+}/Co^{2+} ratios of 1:9, 3:7, 5:5, 7:3 and 9:1, respectively). $Ni_xCo_{1-x}(OH)_2$/NPCs were obtained by washing and drying, noted as $Ni_xCo_{1-x}(OH)_2$/NPC−n, where n = 1, 2, 3, 4 and 5, respectively according to the above order. For comparison, $Ni(OH)_2$/NPC and $Co(OH)_2$/NPC were also prepared.

2.4. Synthesis of activated N-doped porous carbon (ANPC)

NPC and KOH (w/w ratio = 1:2) were mixed in ethanol, dried at 100 °C, and then heated to 700 °C for 2 h at a heating rate of 2 °C min^{-1} under N_2 protection. After washing with 1 mol L^{-1} HCl solution and deionized water, respectively, activated nitrogen-doped porous carbons, denoted as ANPCs, were obtained as the anode of HSC.

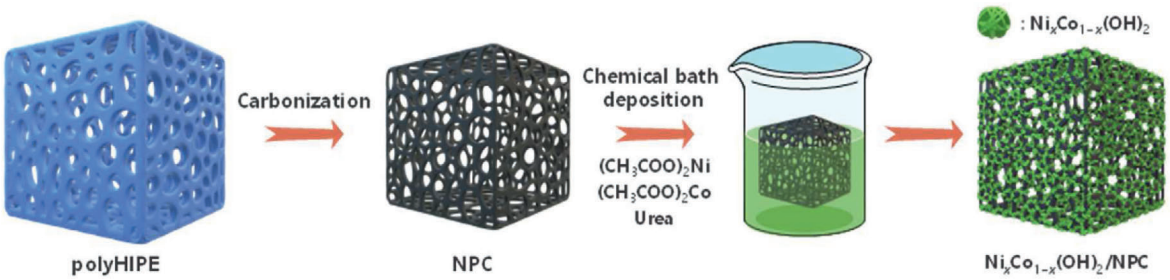

Fig. 1. Schematic illustration for the synthesis of $Ni_xCo_{1-x}(OH)_2$/NPC nanocomposites.

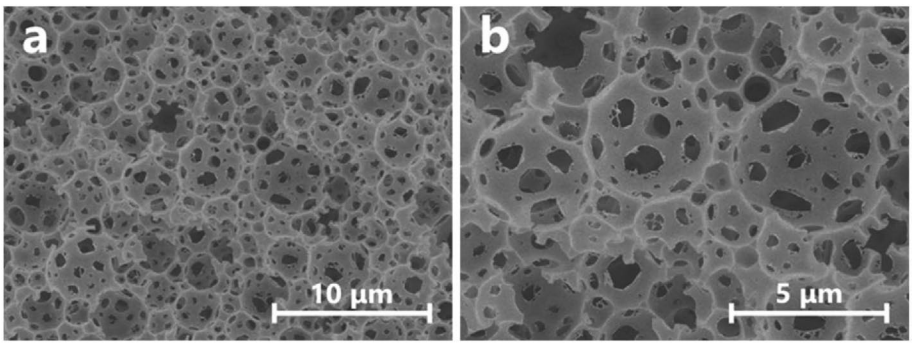

Fig. 2. FESEM images of polyHIPE at different magnifications.

2.5. Instruments and characterization

Field emission scanning electron microscope (FESEM, Hitachi, S-4800, Japan) was used for observing the porous morphology of polyHIPEs, NPCs, and $Ni_xCo_{1-x}(OH)_2$/NPCs. Transmission electron microscope (TEM, FEI, Talos F200X, Czech) was used to observe the microregions of $Ni_xCo_{1-x}(OH)_2$/NPC-5. X-ray diffraction (XRD) was carried out on a PANalytical X'Pert^3 Powder instrument. X-ray photoelectron spectroscopy (XPS) analysis was performed on Thermo Scientific K-Alpha XPS spectrometer. N_2 adsorption/desorption measurements at 77 K were conducted in Quanta chrome ASIQ analyzer.

2.6. Electrochemical measurements

Electrochemical tests were conducted on electrochemical analyzer (CHI660E, Shanghai Chenhua Instruments Co.). For the preparation of working electrodes, the ground $Ni_xCo_{1-x}(OH)_2$/NPC or ANPC powder, acetylene black, and PTFE (8:1:1, w/w/w) were mixed evenly in ethanol via ultrasonic treatment. After drying at 70 °C for 3 h, the obtained slurry was coated on a nickel foam (1.0 × 3.0 cm) and pressed at 10 MPa, then vacuum dried overnight to obtain working electrode.

For a three-electrode system, the Hg/HgO electrode and platinum foil (10 × 10 × 0.1 mm) were used as a reference electrode and a counter electrode, respectively. Cycle voltammetry (CV), galvanostatic charge-discharge (GCD) and electrochemical impedance spectroscopy (EIS, 10 mHz to 100 kHz) were carried out in electrolyte of 6 M of KOH solution. Specific capacitances (C_e, F g^{-1}) were calculated according to the following equation (1) based on the discharge sections of GCD curves, or the following equation (2) based on the CV curves [10,18,42]:

$$C_e = \frac{I\Delta t}{m_e \Delta V} \tag{1}$$

$$C_e = \frac{1}{2m_e \Delta V v}\int_{V_-}^{V_+} I(V)\mathrm{d}V \tag{2}$$

where I (A) is the current, Δt (s) is discharge time, m_e (g) is the mass of active material (namely ANPC or $Ni_xCo_{1-x}(OH)_2$/NPC), ΔV (in V) is the potential change during discharging ($\Delta V = V_+ - V_-$), and v (V s^{-1}) is the scan rate.

2.7. Fabrication of HSCs

To fabricate an HSC device, the $Ni_xCo_{1-x}(OH)_2$/NPC−5 electrode and ANPC electrode were employed as the cathode and anode, respectively. As we mentioned before, the electrodes were assembled into the CR2032 coin-type cell with a piece of non-woven diaphragm (MPF30AC, NKK, Japan) as electrolyte separator (soaked by 6 M KOH in advance) [43]. The mass ratio of $Ni_xCo_{1-x}(OH)_2$/NPC−5 to ANPC was balanced based on the following equation (3) [8]:

$$\frac{m_+}{m_-} = \frac{C_- \Delta V_-}{C_+ \Delta V_+} \tag{3}$$

Moreover, energy density (E, in Wh kg^{-1}) and power density (P, in W kg^{-1}) of $Ni_xCo_{1-x}(OH)_2$/NPC−5//ANPC HSC were calculated according to equations (4) and (5), respectively, based on the discharge sections of GCD curves [6,11]:

$$E = 1/2 \times 1/3.6CV^2 \tag{4}$$

$$P = 3600\frac{E}{\Delta t} \tag{5}$$

Among them, C and V are the specific capacitance and voltage window of HSC, respectively.

3. Results and discussion

3.1. Synthesis and characterization

Herein, $Ni_xCo_{1-x}(OH)_2$/NPC nanocomposites were prepared via a facile two-step route as illustrated in Fig. 1. Firstly, the glitteringly prepared porous polymer through oil in water high internal phase emulsion (HIPE) template was carbonized at high temperature to provide NPC with unique three-dimensional interconnected porous

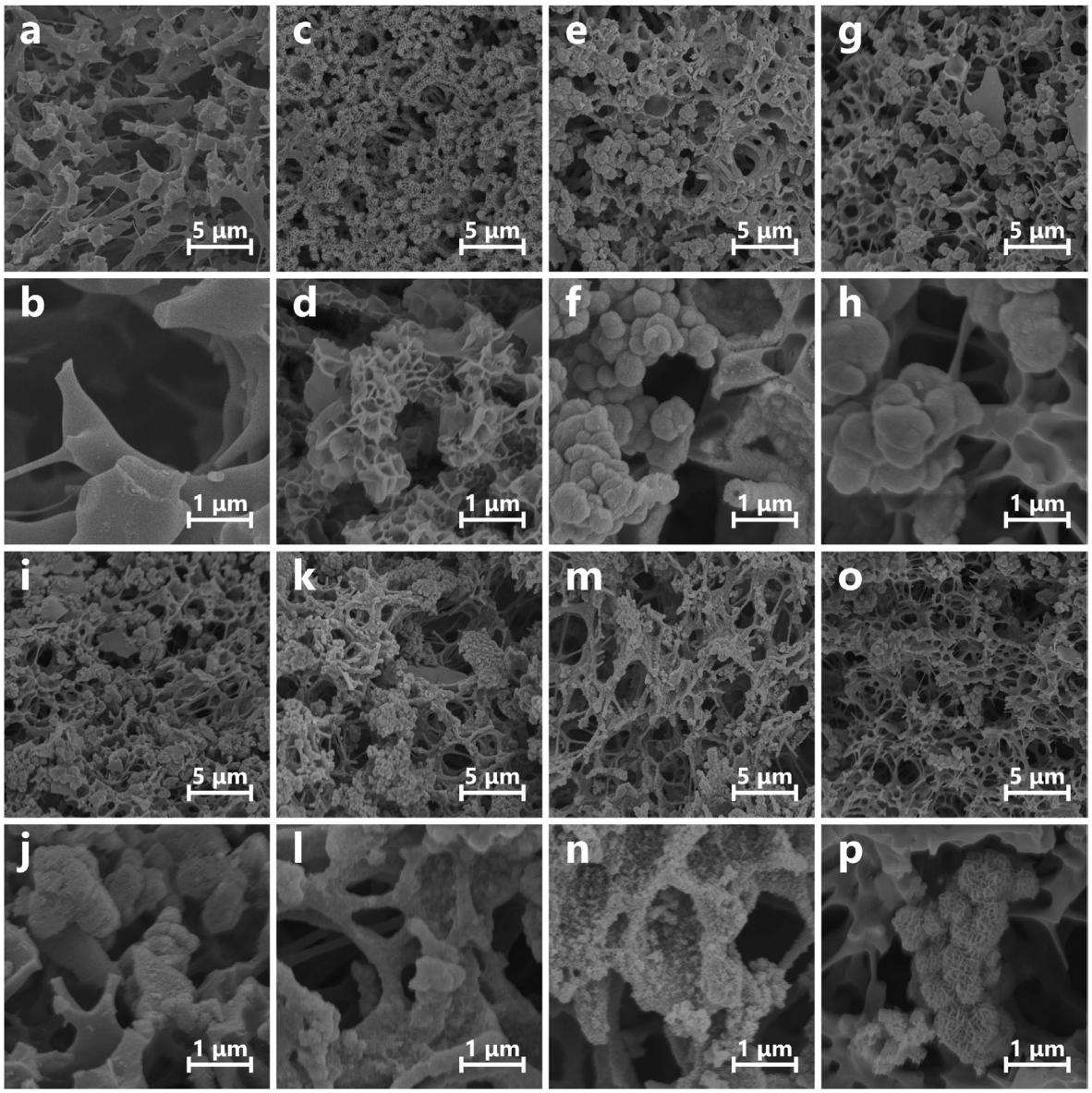

Fig. 3. FESEM images of NPC and $Ni_xCo_{1-x}(OH)_2$/NPCs prepared under different Ni^{2+}/Co^{2+} ratios: (a, b) NPC; (c, d) $Ni(OH)_2$/NPC; (e, f) $Co(OH)_2$/NPC; (g, h) $Ni_xCo_{1-x}(OH)_2$/NPC−1; (i, j) $Ni_xCo_{1-x}(OH)_2$/NPC−2; (k, l) $Ni_xCo_{1-x}(OH)_2$/NPC−3; (m, n) $Ni_xCo_{1-x}(OH)_2$/NPC−4; (o, p) $Ni_xCo_{1-x}(OH)_2$/NPC−5.

structure. Ni,Co bimetallic hydroxide ($Ni_xCo_{1-x}(OH)_2$) was grown on the NPC framework by chemical bath deposition. After washing and drying, $Ni_xCo_{1-x}(OH)_2$/NPC nanocomposites were obtained.

As shown in Fig. 2, the as-prepared polyHIPE has a typical interconnected porous morphology which is beneficial to obtain high available surface area and facilitate ion diffusion. The organic phase xylene which acts as a template for the target porous polymer, leave pores after being removed. The volume shrinkage that occurs during polymerization creates interconnected windows on the pore walls [13,44].

After pyrolysis, the obtained NPC still maintains the porous structure of polyHIPE (Fig. 3a and b). At the same time, the pyrolysis process causes volume shrinkage of the material, which expands the original rough edge window and increases the connectivity. The abundant macroporous structure facilitates the rapid entry of the following chemical bath deposition solution into the interior structure of carbon. It is worth noting that the doping of N can reduce the energy gap of carbon lattice, providing a more convenient path for charge transfer and diffusion of electrolyte ions to provide a faster electrochemical dynamic response [45,46].

FESEM images in Fig. 3 revealed the morphologies of the $Ni_xCo_{1-x}(OH)_2$/NPC composites prepared via chemical bath deposition. It is notable that $Ni_xCo_{1-x}(OH)_2$ nanoparticles or nanoflakes were successfully anchored on the NPC pore walls. Urea can be hydrolyzed into NH_3 and CO_2 to form alkaline solution as equations (6) and (7):

$$CO(NH_2)_2 + H_2O \rightarrow CO_2 + 2NH_3 \cdot H_2O \quad (6)$$

$$NH_3 \cdot H_2O \rightleftharpoons NH_4^+ + OH^- \quad (7)$$

The unique 3D interconnected porous structure and excellent surface area not only facilitates electrolyte diffusion through convenient charge movement routes, but also provides an excellent platform for loading active materials. Benefiting from the enhanced wettability by the N-containing functional groups of NPC, Ni and Co ions tend to aggregate on the surface of NPC pores and combined with the OH^- released during the hydrolysis of urea to form $Ni_xCo_{1-x}(OH)_2$. For the $Ni(OH)_2$/NPC nanocomposite, $Ni(OH)_2$ grows on the pore walls with a flower-like structure composed of nanosheets (Fig. 3c and d), while $Co(OH)_2$ in the $Co(OH)_2$/NPC composite was spherical (Fig. 3e and f). With

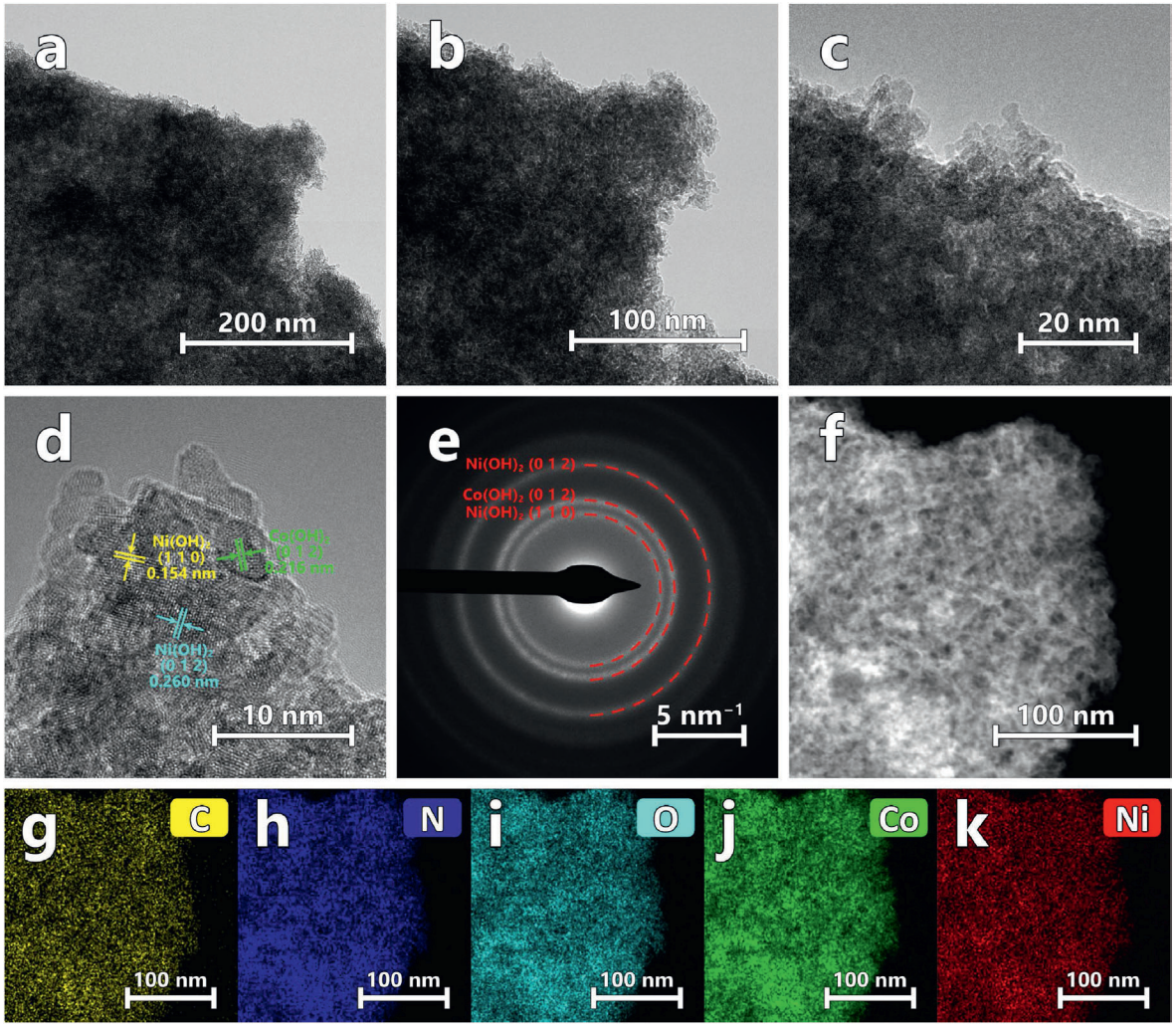

Fig. 4. (a–d) TEM images, (e) SAED pattern and (f) elemental mapping images of $Ni_xCo_{1-x}(OH)_2$/NPC: (g) C, (h) N, (i) O, (j) Co, and (k) Ni.

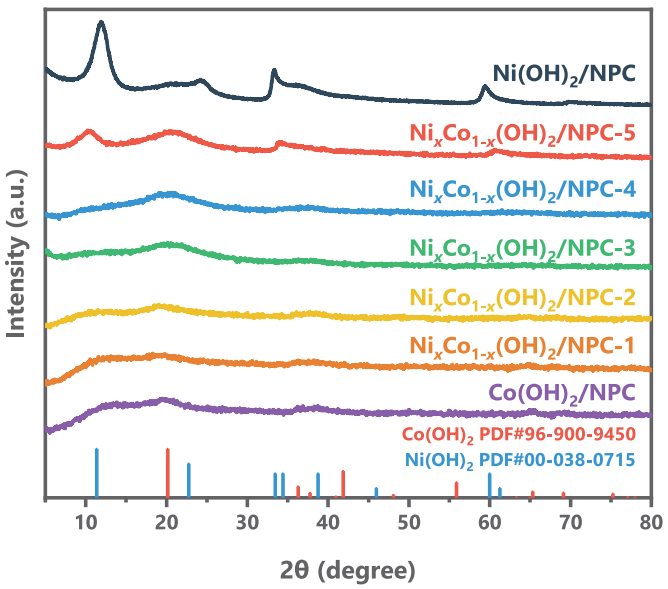

Fig. 5. XRD patterns of $Ni_xCo_{1-x}(OH)_2$/NPCs prepared under different ratios of Ni^{2+}/Co^{2+}.

increasing Ni^{2+}/Co^{2+} ratio, the $Ni_xCo_{1-x}(OH)_2$ of the composite gradually become smaller and smaller particles, at last changed to flower shape.

Further, the detailed microscopic morphology and structure of the $Ni_xCo_{1-x}(OH)_2$/NPC−5 sample were observed by TEM (Fig. 4). Clear lattice edges are shown in the high-resolution TEM image of Fig. 4d. The lattice spacing of 0.216 nm can be indexed to the (0 1 2) plane of Co $(OH)_2$ (PDF#96−900−9450), while the lattice spacings of 0.260 nm and 0.154 nm can be indexed to (0 1 2) and (1 1 0) planes of $Ni(OH)_2$ (PDF#00−038−0715). In addition to the clear crystallites, irregular streaks are also present, which can be attributed to the streaks of amorphous carbon. The SAED diagram shows three diffusion rings, which correspond to the (1 1 0) plane of $Ni(OH)_2$, the (0 1 2) plane of Co $(OH)_2$, and the (0 1 2) plane of $Ni(OH)_2$ from inside to outside. (Fig. 4e).

In the element mapping images shown in Fig. 4g-k, the position of N element basically coincides with that of C element, which proves that N is homogeneously doped in the porous carbon. The distributions of O, Co, and Ni are basically the same, suggesting that the three exist in the form of compounds. Furthermore, they are in good agreement with the shapes of C and N elements, which means that $Ni_xCo_{1-x}(OH)_2$ nanostructures distribute evenly on the whole carbon.

In order to further reveal the composition and crystal structure of the samples, their XRD patterns were collected in Fig. 5. For $Ni(OH)_2$/NPC, the clear diffraction peaks can be well matched to the α−$Ni(OH)_2$ crystal phase (PDF#00−038−0715) [8,18]. The four main diffraction peaks of $Ni(OH)_2$/NPC at 11.4°, 22.7°, 34.4° and 60.0°, corresponding to (0 0 3),

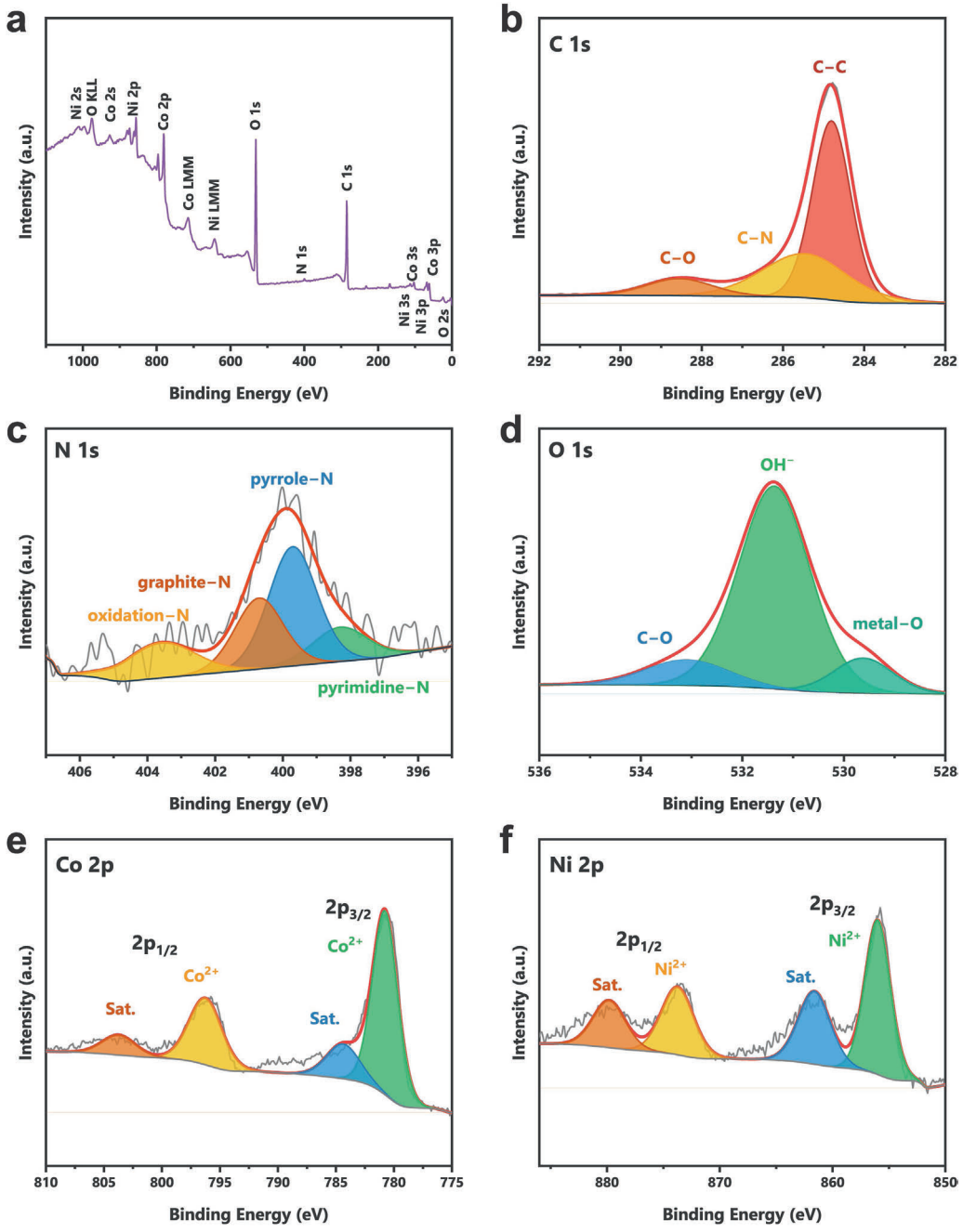

Fig. 6. XPS survey spectra of $Ni_xCo_{1-x}(OH)_2$/NPC−5: (a) full spectrum; (b) C 1s; (c) N 1s; (d) O 1s; (e) Co 2p; (f) Ni 2p.

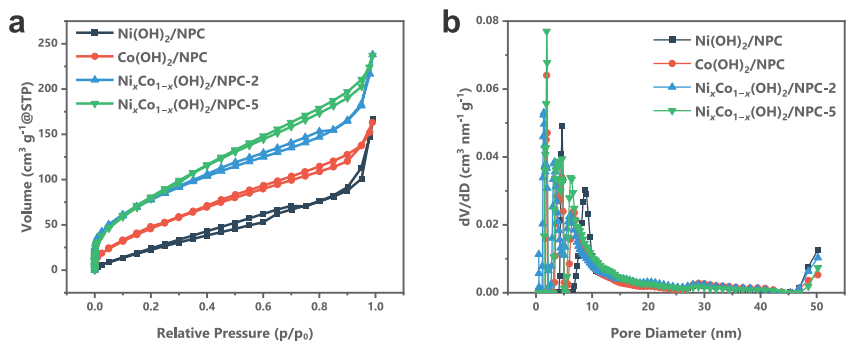

Fig. 7. (a) N_2 adsorption/desorption isotherms and (b) pore size distributions of $Ni_xCo_{1-x}(OH)_2$/NPCs.

Table 1
Surface areas and pore properties of $Ni_xCo_{1-x}(OH)_2$/NPCs.

Sample	S_{BET} ($m^2\ g^{-1}$)	V_{total} ($cm^3\ g^{-1}$)	$D_{average}$ (nm)
$Ni(OH)_2$/NPC	88	0.187	1.678
$Co(OH)_2$/NPC	129	0.207	1.915
$Ni_xCo_{1-x}(OH)_2$/NPC−2	190	0.267	1.915
$Ni_xCo_{1-x}(OH)_2$/NPC−5	209	0.273	1.416

(0 0 6), (0 1 2) and (1 1 0) planes, respectively. Since the synthesized Co$(OH)_2$ does not have a significantly sharp geometry but a spherical structure, the diffraction peaks of $Co(OH)_2$/NPC are not very clear, but the diffraction peaks at 20.2° and 36.3° can still be observed, corresponding to the (0 0 2) and (0 1 0) planes (PDF#96−900−9450), indicating the low crystallinity. For other samples, the diffraction peak intensities increased with increasing Ni content, which is corresponded to the topographic changes by SEM.

The chemical composition of $Ni_xCo_{1-x}(OH)_2$/NPC−5 was investigated by XPS analysis (Fig. 6). Fig. 6a indicated that $Ni_xCo_{1-x}(OH)_2$/NPC−5 is composed of C, N, O, Co and Ni elements. In the high-resolution C 1s spectrum (Fig. 6b), the peaks at 284.8, 285.5 and 288.6 eV are assigned to C−C, C−N and C−O bonds, respectively. Four characteristic peaks of the N 1s spectrum were fitted at 398.3, 399.7, 400.7 and 403.6 eV, corresponding to pyrimidine−N, pyrrole−N, graphitic−−−N, and oxide−N, respectively (Fig. 6c) [47]. Pyrimidine-N contributes to higher electronic conductivity and faster charge transfer. Pyrrole-N can participate in reversible Faraday reactions and provide

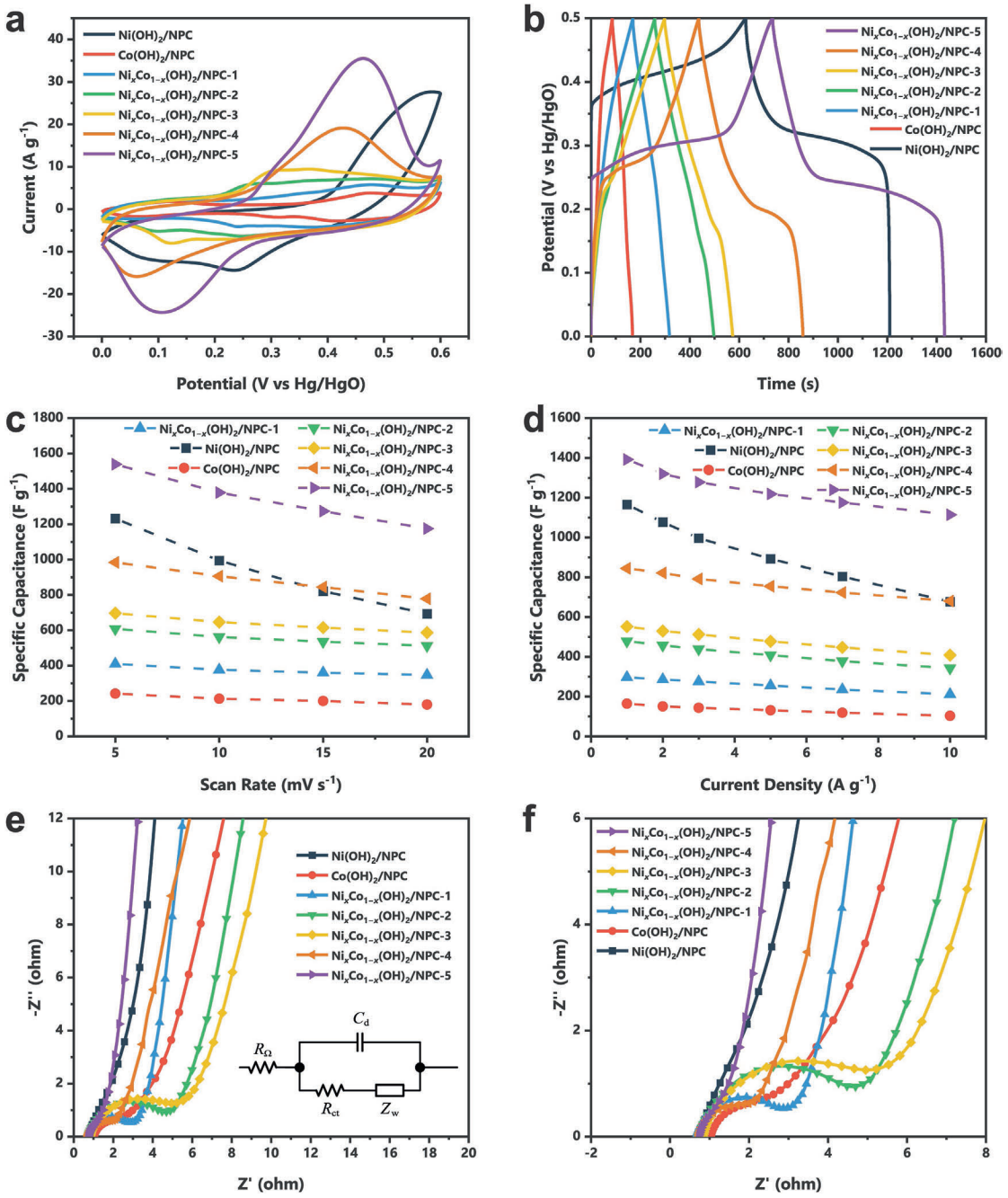

Fig. 8. Electrochemical properties of $Ni_xCo_{1-x}(OH)_2$/NPCs in a three−electrode system in 6 mol L^{-1} KOH: (a) CV curves at 10 mV s^{-1}; (b) GCD curves at 1 A g^{-1}; (c) specific capacitance at different scan rates; (d) specific capacitance at different current densities; (e) Nyquist plots (inset: the equivalent electrical circuits used for fitting the impedance spectra); (f) the magnified image at higher frequency region of Nyquist plots.

Table 2
Rate performance of $Ni_xCo_{1-x}(OH)_2$/NPC electrodes.

Sample	Capacitance (F/g)		Rate performance (%)	
	GCD (1 A/g)	CV (10 mV/s)	from GCD (1–10 A/g)	From CV (5–20 mV/s)
$Ni(OH)_2$/NPC	1166	994.7	58.05	56.27
$Co(OH)_2$/NPC	164.2	212.8	62.97	74.38
$Ni_xCo_{1-x}(OH)_2$/NPC−1	296.9	376.3	71.27	84.78
$Ni_xCo_{1-x}(OH)_2$/NPC−2	478.5	562.5	71.60	84.25
$Ni_xCo_{1-x}(OH)_2$/NPC−3	552.0	646.3	73.99	84.24
$Ni_xCo_{1-x}(OH)_2$/NPC−4	844.2	906.1	80.60	79.08
$Ni_xCo_{1-x}(OH)_2$/NPC−5	1392	1379	80.03	76.35

Table 3
The EIS fitting results of $Ni_xCo_{1-x}(OH)_2$/NPCs.

Sample	R_Ω (Ω)	R_{ct} (Ω)
$Ni(OH)_2$/NPC	0.789	1.970
$Co(OH)_2$/NPC	1.110	0.593
$Ni_xCo_{1-x}(OH)_2$/NPC−1	0.770	1.411
$Ni_xCo_{1-x}(OH)_2$/NPC−2	0.835	2.389
$Ni_xCo_{1-x}(OH)_2$/NPC−3	0.954	2.631
$Ni_xCo_{1-x}(OH)_2$/NPC−4	0.787	0.892
$Ni_xCo_{1-x}(OH)_2$/NPC−5	0.826	0.828

additional pseudocapacitance. The presence of graphite-N also contributes to conductivity [41].

The high content of N doping is also beneficial to increase the hydrophilicity and the growth probability of $Ni_xCo_{1-x}(OH)_2$. The peaks at 529.6, 531.4 and 533.1 eV in the O 1s spectrum are assigned to metal−O, OH^- and C−O bonds (Fig. 6d). For the high-resolution Co 2p spectrum (Fig. 6e), the characteristic peaks of Co $2p_{3/2}$ and Co $2p_{1/2}$ can be bimodal fitted: the spin-orbit doublets at 780.8 and 796.2 eV can be attributed to the Co^{2+} of $Co(OH)_2$, the two peaks at 784.4 and 803.7 eV can be attributed to satellite peaks [48]. The high-resolution Ni 2p XPS spectrum (Fig. 6f) shows characteristic peaks of Ni $2p_{3/2}$ and Ni $2p_{1/2}$, attributed to Ni^{2+} of $Ni(OH)_2$ (856.0 and 873.7 eV) and satellite peaks (861.6 and 879.8 eV) according to doublet fitting [48].

XPS spectra showed that Ni and Co existed mainly in their divalent ion forms, respectively, while the strong OH^- peaks in O 1s spectra also proved the existence of $Co(OH)_2$ and $Ni(OH)_2$, which was consistent with XRD and EDS results.

The pore structures of the samples were studied by N_2 adsorption/desorption isotherms measured by the DFT method, as shown in Fig. 7. According to the IUPAC classification method, $Ni_xCo_{1-x}(OH)_2$/NPC shows a typical IV(a) type isotherm [49]. The rapid growth of the isotherm at lower relative pressures proves the presence of a certain amount of micropores (Fig. 7a); while the H3-type hysteresis loop on the curve indicates the presence of well-developed mesopores inside the material [8]. In addition, the upward curve at the end of the isothermal curve verifies the presence of a macroporous structure. The pore size distribution diagram (Fig. 7b) shows that $Ni_xCo_{1-x}(OH)_2$/NPC has a large number of mesopores, as well as a certain amount of micropores, which is consistent with the N_2 adsorption and desorption curves. The hierarchical porous structure with interconnected macropores, mesopores and micropores provides a high specific surface area with a large number of electrochemically active sites, which can effectively increase the electrochemical performance of the electrode material.

The pore structure parameters of $Ni_xCo_{1-x}(OH)_2$/NPC are summarized in Table 1. $Co(OH)_2$/NPC has a higher specific surface area compared to $Ni(OH)_2$/NPC. There is a significant increase in the specific surface area for $Ni_xCo_{1-x}(OH)_2$/NPC, due to the intercalation structure between $Co(OH)_2$ and $Ni(OH)_2$, which will prevent them from forming crystalline structures, while maintaining abundant micropores and high specific surface area.

3.2. Electrochemical performance of $Ni_xCo_{1-x}(OH)_2$/NPC electrodes

The electrochemical capacitive properties of $Ni_xCo_{1-x}(OH)_2$/NPC electrodes were evaluated in a three-electrode system. The CV and GCD curves of $Ni_xCo_{1-x}(OH)_2$/NPC electrodes are shown in Fig. 8a and b, respectively. A pair of asymmetric redox peaks indicates mainly a diffusion controlled charge storage mechanism for $Ni(OH)_2$/NPC electrode, which is also evidenced by the obvious charging and discharging plateaus on its GCD curve. In contrast, the symmetric redox peaks appearing on the CV curve of $Co(OH)_2$/NPC electrode imply a pseudocapacitive process with only a slight bending in its GCD curve.

The redox reaction at the $Ni_xCo_{1-x}(OH)_2$/NPC electrode may consist of the following equations [8]:

$$Ni(OH)_2 + OH^- \rightleftharpoons NiOOH + H_2O + e^- \quad (8)$$

$$Co(OH)_2 + OH^- \rightleftharpoons CoOOH + H_2O + e^- \quad (9)$$

$$CoOOH + OH^- \rightleftharpoons CoO_2 + H_2O + e^- \quad (10)$$

The specific capacitances calculated using equations (1) and (2) according to the CV curves and GCD curves are plotted in Fig. 8c and d, respectively. Their specific capacitances and rate performances are calculated respectively and summarized in Table 2. It can be seen that although the specific capacitance of $Ni(OH)_2$/NPC electrode is high, its rate performance of only 58.05 % makes it difficult to meet the requirements of HSC at higher loads. The $Co(OH)_2$/NPC electrode, as a pseudo-capacitance electrode, has the advantage of better rate performance, but its lower specific capacitance results in lower energy density of HSC. As the Ni^{2+}/Co^{2+}ratio increases, the cobalt content of $Ni_xCo_{1-x}(OH)_2$/NPC gradually decreases while nickel content gradually increases. These $Ni_xCo_{1-x}(OH)_2$/NPC electrodes exhibits pseudocapacitance/Faraday combined mechanism for energy storage and tend to change to a battery-type electrode with the increase of Ni^{2+}/Co^{2+}ratio, e.g. $Ni_xCo_{1-x}(OH)_2$/NPC−4 and $Ni_xCo_{1-x}(OH)_2$/NPC−5.

The specific capacitance of the $Ni_xCo_{1-x}(OH)_2$/NPC electrode gradually enhanced with increasing nickel content, reaching to a maximum of 1392 F g^{-1} at a Ni^{2+}/Co^{2+} molar ratio of 9:1 ($Ni_xCo_{1-x}(OH)_2$/NPC−5), while still maintaining 80 % of the initial capacitance with current density increasing from 1 to 10 A g^{-1}. The introduced Co^{2+} partially replaces the Ni^{2+} positions in $Ni(OH)_2$, creating structural defects and exposing lots of reactive sites, meanwhile Co^{2+} also act synergistically as active sites [11]. The increase in cobalt content lowers the charge/discharge plateau of the electrode, which helps the battery-type electrode to store/release electrical energy faster and more fully at high current densities/scan rates, which is beneficial for the electrode rate performance.

The Nyquist plots of the electrodes are shown in Fig. 8e and f, to investigate the conductive properties of the electrodes. As shown in the inset of Fig. 8e, the equivalent circuit model consists of internal resistance (R_Ω), capacitance (C_d), charge transfer resistance (R_{ct}), and Warburg resistance (Z_W). The R_Ω and R_{ct} of all $Ni_xCo_{1-x}(OH)_2$/NPC electrodes are listed in Table 3. $Ni_xCo_{1-x}(OH)_2$/NPC−1, $Ni_xCo_{1-x}(OH)_2$/NPC−2 and $Ni_xCo_{1-x}(OH)_2$/NPC−3 electrodes exhibit the characteristics of capacitive electrodes, where the charge transfer

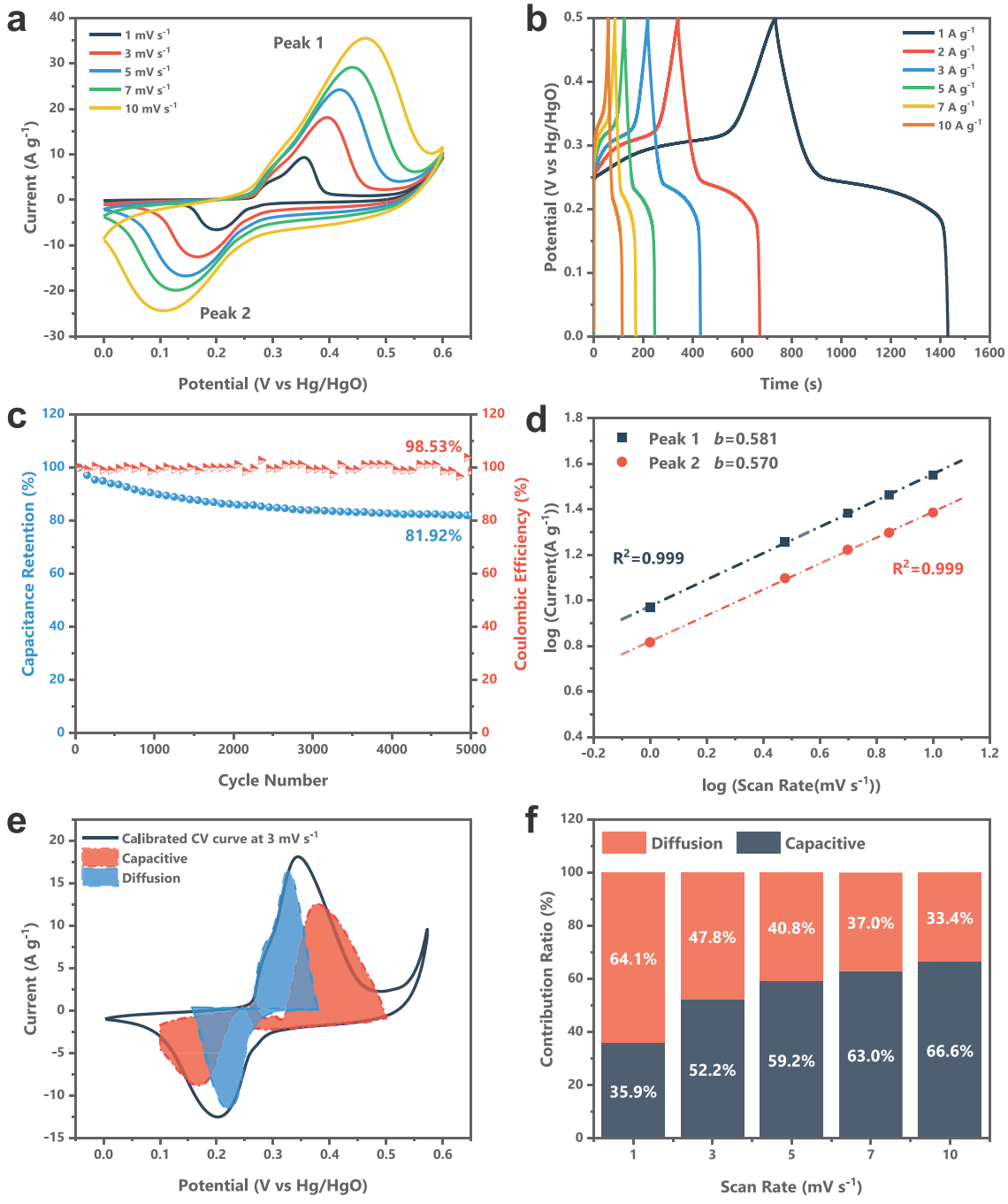

Fig. 9. Electrochemical properties of $Ni_xCo_{1-x}(OH)_2$/NPC−5 electrode: (a) CV curves; (b) GCD curves; (c) cycling stability based on GCD study; (d) plots of log (peak current) versus log (scan rate); (e) the capacitive and diffusion contribution at 1 mV s^{-1}; (f) the capacitive and diffusion contribution ratios.

dominates significantly in the high frequency region with a distinct semicircular region at relatively low Ni^{2+}/Co^{2+} ratio. As the Ni^{2+}/Co^{2+} ratio increases, the R_{ct} increases significantly, which leads to a decrease in the rate performance of the electrode. The Nyquist plots exhibit battery-type characteristics with small semicircular curves in the high-frequency region, suggesting low charge transfer resistance, but significant transfer control in the low-frequency region. For $Ni_xCo_{1-x}(OH)_2$/NPC−5 electrode, the slope in the low-frequency region is steeper, indicating lower transfer resistance.

The $Ni_xCo_{1-x}(OH)_2$/NPC−5 electrode exhibited the highest specific capacitance while maintaining good rate performance, so was selected for further investigations (Fig. 9a and b). With increasing scan rates from 1 to 10 mV s^{-1} and current densities from 1 to 10 A g^{-1}, the shapes of the CV and GCD curves maintain excellent agreement, respectively, further confirming the excellent capacitance retention stability. In addition, the durability of the $Ni_xCo_{1-x}(OH)_2$/NPC−5 electrode was verified by continuous GCD recycling experiments at 10 A g^{-1} (Fig. 9c). The performance of the $Ni_xCo_{1-x}(OH)_2$/NPC−5 electrode gradually decayed as the recycling proceeded, eventually maintained a capacitance of 81.9 % and a Coulombic efficiency of 98.5 %. This can be attributed to the anchoring effect of the pores of NPC, which hinders the agglomeration of $Ni_xCo_{1-x}(OH)_2$, and thus improves its stability and cycling performance.

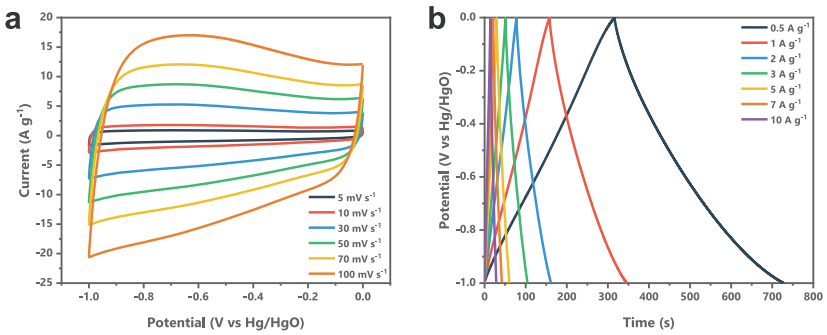

Fig. 10. Electrochemical measurements of the ANPC electrode: (a) CV curves; (b) GCD curves.

The Co doping also reduces the charge transfer resistance and improves the cycling stability [38].

To deeply explore the battery/pseudocapacitor energy storage kinetics of the electrode material, a semi-quantitative analysis of capacitance effects is performed according to the relationship between current density (i) and scan rates (v), as in equation (11) [50,51]:

$$i = av^b \tag{11}$$

where a and b are variable parameters.

If the value of b is 0.5, the electrode material behaves as a battery property (controlled by diffusion behavior); if the value of b is 1, the electrode material exhibits pseudo-capacitance properties (controlled by capacitive behavior). In this case, the fitted b values are 0.581 and 0.570 for the oxidation and reduction peaks (peak 1 and peak 2, respectively) (Fig. 9d), which demonstrates that $Ni_xCo_{1-x}(OH)_2$/NPC−5 exhibits battery as well as pseudocapacitance properties. The quantitative capacitance contribution is calculated by the following equation (12) [50–52]:

$$i(V) = k_1 v + k_2 v^{1/2} \tag{12}$$

where k_1 and k_2 are constant parameters, and $i(V)$ is the current density at the corresponding voltage (V).

Briefly, $k_1 v$ points out the capacitive-controlled contribution, and $k_2 v^{1/2}$ points out the diffusion-controlled contribution. Fig. 9e presents the calculated capacitive-controlled fraction and diffusion-controlled fraction of the $Ni_xCo_{1-x}(OH)_2$/NPC−5 electrode at 3 mV s^{-1} after calibration [52]. The capacitive-controlled contribution ratio reaches 35.9 %, and as the scan rate increases to 10 mV s^{-1}, the ratio reaches 66.6 % (Fig. 9f).

3.3. Electrochemical performance of $Ni_xCo_{1-x}(OH)_2$/NPC-5//ANPC HSC

For further evaluating the actual performance of the $Ni_xCo_{1-x}(OH)_2$/NPC−5 electrode in practical applications, an HSC was fabricated with ANPC as the anode. It should be emphasized that ANPC is obtained by KOH activation treatment of NPC, which means ANPC has a higher porosity and higher SSA, which is benefit to improve electron exchange and electrolyte ion transport. The CV curves (Fig. 10a) of ANPC electrode basically show a rectangular-like shape, implying an energy storage mechanism of double-layer capacitance. Also, the slight, especially between −0.8 ~ −0.4 V, implies an accompanying partial pseudocapacitance provided by the rapid redox reactions of the N-containing functional groups at the interface of the electrode material and the electrolyte [53]. The specific capacitance of ANPC is calculated as 205.5 F g^{-1} at 0.5 A g^{-1} (Fig. 10b).

It is reasonable to select 0–1.6 V as the operating voltage window for the HSC based on the aforementioned CV curves of the $Ni_xCo_{1-x}(OH)_2$/NPC−5 electrode (Fig. 9a) and ANPC (Fig. 10a), as further confirmed by the CV curves of the HSC in Fig. 11b. And the CV curves of $Ni_xCo_{1-x}(OH)_2$/NPC−5//ANPC HSC have excellent shape consistency as the scan rate increases from 10 to 100 mV S^{-1} (Fig. 11b), indicating that the HSC has good capacitance retention stability and can maintain good charge/discharge performance at high scan rates. From the GCD curves in Fig. 11c, the specific capacitances of HSC are 334.4, 287.4, 258.5, 238.5, 212.1, 180.1, and 136.5 F g^{-1} at 0.5, 1, 2, 3, 5, 7, and 10 A g^{-1}, respectively (Fig. 11d), and the rate performance at high current density was 40.8 %.

According to equations (4) and (5), the $Ni_xCo_{1-x}(OH)_2$/NPC−5//ANPC HSC possesses a maximum energy density of 118.9 Wh kg^{-1} at 400.0 W kg^{-1} and a maximum power density of 8201 W kg^{-1} at 48.52 Wh kg^{-1} (Fig. 11e). What is more, compared with similar composite material assembled HSC previously reported [54–61], the HSC we assembled still exhibit relatively appreciable energy density at a definite power density. Similarly, the durability of $Ni_xCo_{1-x}(OH)_2$/NPC−5//ANPC HSC was studied by GCD cycling at 10 A g^{-1} (Fig. 11f). The performance of the HSC decayed rapidly in the first 500 cycles, but remained stable for the next 4500 cycles and finally stabilized at 80.7 % of the original performance. The Coulomb efficiency remained stable, reaching 97.4 % after 5000 cycles.

To further test the practical application potential of the assembled HSC which was schematically shown in Fig. 12a, two series-connected $Ni_xCo_{1-x}(OH)_2$/NPC−5//ANPC HSCs were used to power an LED (2 V) and their duration was recorded (Fig. 12b). The two tandem HSCs maintained a high output power with high LED brightness for the first 90 s. After that, they maintained a low power output, but the total output voltage was kept above the rated voltage of the LED for ~7 min.

4. Conclusions

In conclusion, $Ni_xCo_{1-x}(OH)_2$/NPC nanocomposites were prepared for hybrid supercapacitors via an elaborated two-step synthesis route, i.e. HIPE templating together with CBD. NPC with interconnected porous architecture was synthesized by HIPE templating while nanostructured $Ni_xCo_{1-x}(OH)_2$ were loaded onto the NPC surface via CBD. The unique 3D porous morphology of NPC not only provides large accessible area and convenient charge movement routes for electrolyte diffusion, but also acts as an conductive platform for growth and anchors of $Ni_xCo_{1-x}(OH)_2$ without agglomeration. The introduction of Co not only improve the specific surface area and porosity of the nanocomposites, but also formed more structural defects and active sites. The optimized $Ni_xCo_{1-x}(OH)_2$/NPC−5 electrode combines a high specific capacitance of 1392 F g^{-1} (at 1 A g^{-1}) and excellent high rate performance of 80.0 %. The assembled HSC of $Ni_xCo_{1-x}(OH)_2$/NPC−5//ANPC has an impressive energy density of maximum 118.9 Wh kg^{-1} at 400.0 W kg^{-1}, with a capacitance retention rate of 80.7 % after 5000 cycles, enabling stable power output in practical load applications. This work provides new

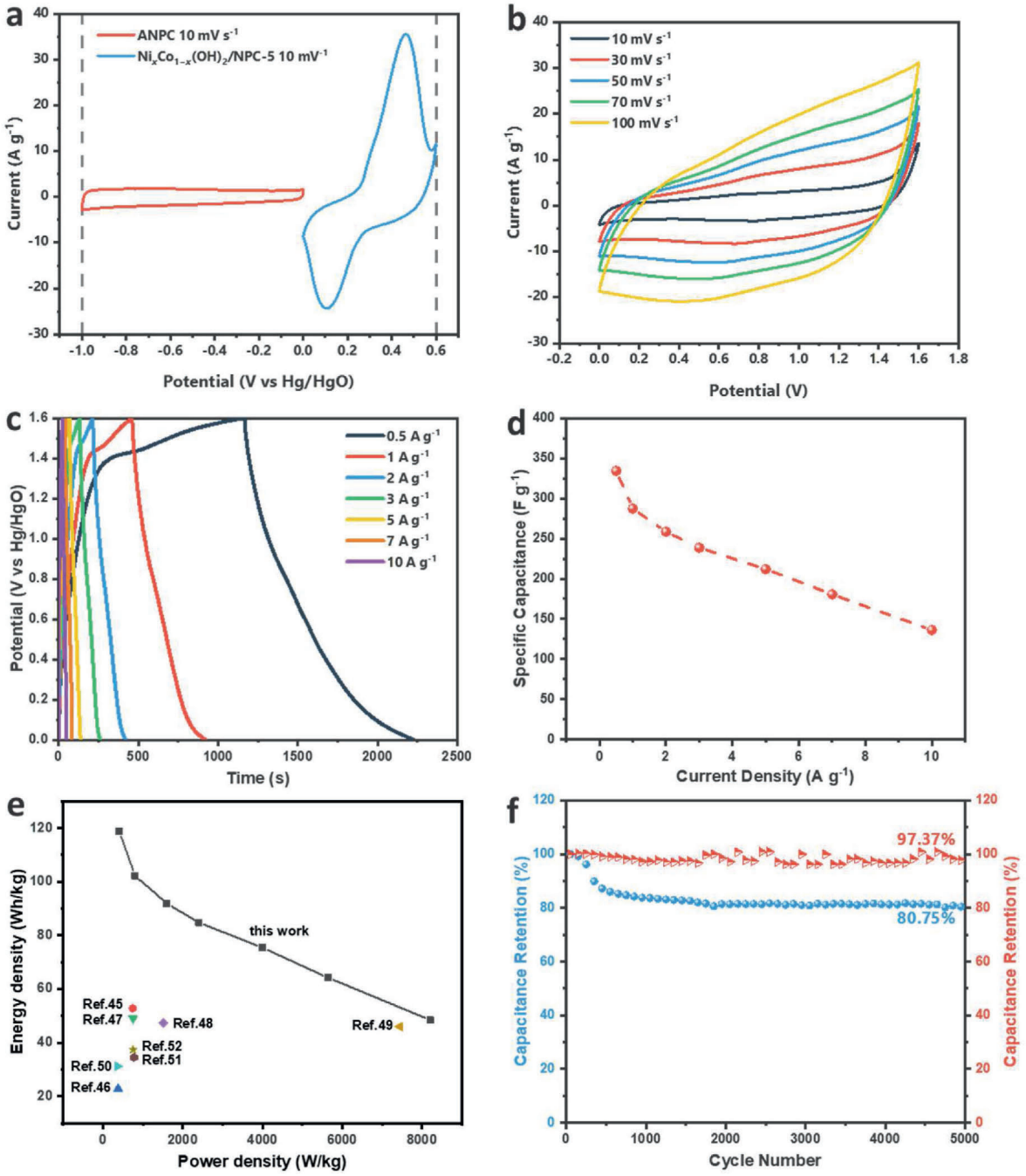

Fig. 11. Electrochemical properties of $Ni_xCo_{1-x}(OH)_2$/NPC−5//ANPC: (a) CV curves of $Ni_xCo_{1-x}(OH)_2$/NPC−5 and ANPC electrode at 10 mV s^{-1}; (b) CV curves, (c) GCD curves, (d) calculated capacitances at 0.5–10 A g^{-1}, (e) Ragone plots (comparison with other reports), and (f) cyclic property at 10 A g^{-1} of $Ni_xCo_{1-x}(OH)_2$/NPC−5//ANPC HSC.

inspirations for the reasonable design of novel and superior electrode materials for first-rate hybrid supercapacitors.

CRediT authorship contribution statement

Yulai Zhao: Writing – review & editing, Supervision, Funding acquisition. **Yuxuan Chen:** Formal analysis, Conceptualization. **Haoran Chen:** Writing – original draft, Investigation, Data curation. **Longqiang Xiao:** Conceptualization, Data curation. **Xuehui Ge:** Writing – review & editing, Methodology, Conceptualization. **Xiangyu Yin:** Supervision, Data curation. **Linxi Hou:** Supervision, Resources, Conceptualization.

Declaration of competing interest

The authors declare that they have no known competing financial interests or personal relationships that could have appeared to influence the work reported in this paper.

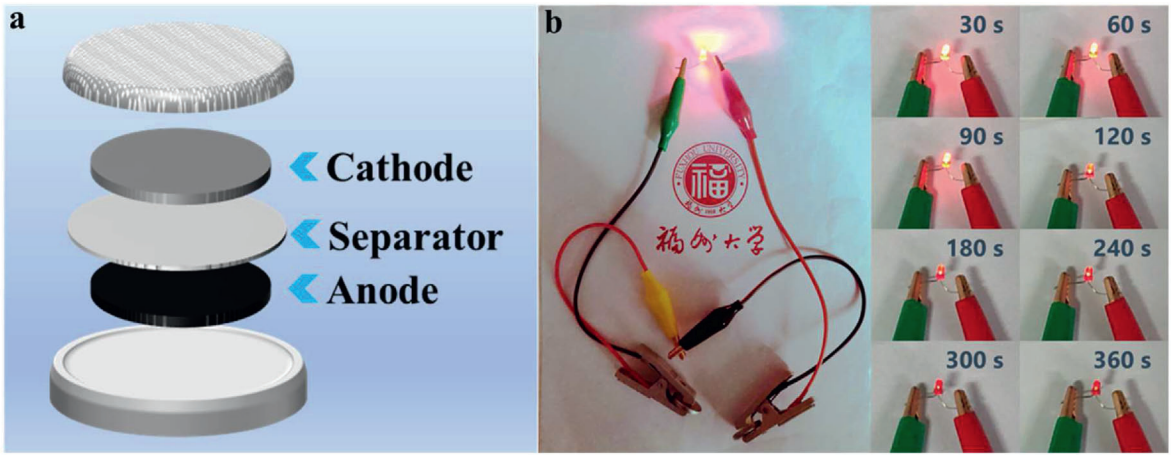

Fig. 12. (a) The schematic diagram of HSC, (b) Photograph of a red LED lighted by two as-prepared HSCs in series.

Acknowledgment

We gratefully acknowledge the financial supports from the Natural Science Foundation of Fujian province (No. 2022J01569), National Natural Science Foundation of China (No. U21A20313), Major Program of Qingyuan Innovation Laboratory (No. 00122004), Key Program of Qingyuan Innovation Laboratory (No. 00221003) and '111' program of Fuzhou University, for financial supports.

References

[1] J.Y. Heo, R. Vinodh, H.-J. Kim, R.S. Babu, K.K. Kumar, C.V.V.M. Gopi, et al., Template and binder free 1D cobalt nickel hydrogen phosphate electrode materials for supercapacitor application, J. Ind. Eng. Chem. 106 (2022) 328–339.
[2] H. Zhu, X. Sun, H. Yang, Ya Pang, S. Ta, L. Wang, et al., Polydopamine-derived nitrogen-doped carbon-coated NiS nanoparticles as a battery-type electrode for high-performance supercapacitors, Ceram. Int. 47 (7) (2021) 9332–9341.
[3] G.Z. Chen, Supercapacitor and supercapattery as emerging electrochemical energy stores, Int. Mater. Rev. 62 (4) (2017) 173–202.
[4] S.N.L.M. Chakraborty, Review—an overview on supercapacitors and its applications, J. Electrochem. Soc. 169 (2) (2022) 020552.
[5] Y. Dahiya, M. Hariram, M. Kumar, A. Jain, D. Sarkar, Modified transition metal chalcogenides for high performance supercapacitors: current trends and emerging opportunities, Coord. Chem. Rev. 451 (2022) 214265.
[6] T. Guo, D. Zhou, L. Pang, S. Sun, T. Zhou, J. Su, Perspectives on working voltage of aqueous supercapacitors, Small 18 (16) (2022) 2106360.
[7] H. Xiao, Y. Ma, M. Xu, R. Liu, X. Li, X. Wang, et al., Constructing nickel cobaltate@nickel-manganese layered double hydroxide hybrid composite on carbon cloth for high-performance flexible supercapacitors, J. Colloid Interface Sci. 611 (2022) 149–160.
[8] L. Jing, L. Zhang, G. Li, Z. Guo, Z. Li, Z. Li, et al., Rapid and large-scale synthesis of polydopamine based N-doped carbon spheres@$Co_xNi_{1-x}(OH)_2$ core-shell nanocomposites for high performance supercapacitors, J. Alloys Compd. 854 (2021) 157246.
[9] S. Chen, H. Yu, L. Chen, H. Jiang, C. Li, Defect-domains enabling VO_2 nanosheet arrays with fast charge transfer for 3.0 V aqueous supercapacitors, Chem. Eng. J. 423 (2021) 130208.
[10] J. Zhang, X.S. Zhao, On the configuration of supercapacitors for maximizing electrochemical performance, ChemSusChem 5 (5) (2012) 818–841.
[11] Y. Chen, Q. Ren, X. Zhou, H. Ji, Recent advances in porous organic polymers for the synthesis of cyclic carbonates from carbon dioxide, Chem. Ind. Eng. Prog. 40 (7) (2021) 3564–3583.
[12] S. Dai, Y. Bai, W. Shen, S. Zhang, H. Hu, J. Fu, et al., Core-shell structured Fe_2O_3@Fe_3C@C nanochains and Ni–Co carbonate hydroxide hybridized microspheres for high-performance battery-type supercapacitor, J. Power Sources 482 (2021) 228915.
[13] W. Hu, F. Xie, Y. Li, Z. Wu, K. Tian, M. Wang, et al., Hierarchically porous carbon derived from PolyHIPE for supercapacitor and deionization applications, Langmuir 33 (46) (2017) 13364–13375.
[14] M. Xie, Z. Xu, S. Duan, Z. Tian, Y. Zhang, K. Xiang, et al., Facile growth of homogeneous $Ni(OH)_2$ coating on carbon nanosheets for high-performance asymmetric supercapacitor applications, Nano Res. 11 (1) (2018) 216–224.
[15] M. Xie, S. Duan, Y. Shen, K. Fang, Y. Wang, M. Lin, et al., In-Situ-grown $Mg(OH)_2$-Derived hybrid α-$Ni(OH)_2$ for highly stable supercapacitor, ACS Energy Lett. 1 (4) (2016) 814–819.
[16] X. Wang, A. Hu, C. Meng, C. Wu, S. Yang, X. Hong, Recent advance in Co_3O_4 and Co_3O_4-containing electrode materials for high-performance supercapacitors, Molecules 25 (2) (2020) 269.
[17] X.-M. Yue, Z.-J. Liu, C.-C. Xiao, M. Ye, Z.-P. Ge, C. Peng, et al., Synthesis of Co_3O_4/reduced graphene oxide by one step-hydrothermal and calcination method for high-performance supercapacitors, Ionics 27 (1) (2021) 339–349.
[18] C. Chen, M. Liu, Z. Liu, M. Xie, L. Wan, J. Chen, et al., Design of mesoporous Ni-Co hydroxides nanosheets stabilized by BO_2 for pseudocapacitors with superior performance, J. Colloid Interface Sci. 614 (2022) 66–74.
[19] C. Young, J. Kim, Y.V. Kaneti, Y. Yamauchi, One-step synthetic strategy of hybrid materials from bimetallic metal–organic frameworks for supercapacitor applications, ACS Appl. Energy Mater. 1 (5) (2018) 2007–2015.
[20] C. Xiong, W. Cao, Q. Long, J. Chen, Y. Yu, X. Lian, et al., Etching-induced ion exchange engineering of two-dimensional layered NiFeCo-based hydroxides for high energy charge storage, Dalton Trans. 53 (3) (2024) 1295–1306.
[21] W. Cao, W. Zhao, C. Xiong, Q. Long, N. Chen, G. Du, NiCo-MOF derived nanostructured NiCo-LDH@$Ni(OH)_2$ heterogeneous composite as electrode material for hybrid supercapacitors, J. Energy Storage 64 (2023) 107213.
[22] Wei Cao, Chenhan Xiong, Yu Liu, Fang Xu, Wenjing Zhao, et al., Novel fabrication strategy of nanostructured NiCo-LDHs monolithic supercapacitor electrodes via inducing electrochemical in situ growth on etched nickel foams, J. Alloys Compd. 902 (2022) 163679.
[23] X. Wang, H. Song, S. Ma, M. Li, G. He, M. Xie, et al., Template ion-exchange synthesis of Co-Ni composite hydroxides nanosheets for supercapacitor with unprecedented rate capability, Chem. Eng. J. 432 (2022) 134319.
[24] Y. Yao, Y. Yu, L. Wan, C. Du, Y. Zhang, J. Chen, et al., Structurally-stable Mg-Co-Ni LDH grown on reduced graphene by ball-milling and ion-exchange for highly-stable asymmetric supercapacitor, J. Colloid Interface Sci. 649 (2023) 519–527.
[25] Y. Yao, H. Li, Y. Yu, C. Du, L. Wan, H. Ye, et al., Stabilizing microstructure of Co-Ni layered double hydroxides by magnesium doping and confinement in carbonaceous mesopores for ultrahighly-stable asymmetric supercapacitor, J. Energy Storage 59 (2023) 106422.
[26] D.K. Mohapatra, S. Praharaj, D. Rout, Electrochemical charge storage performance of mesoporous MoO_3@Co_3O_4 nanocomposites as electrode materials, Nanotechnology 33 (15) (2022) 155709.
[27] Z. Ji, K. Liu, N. Li, H. Zhang, W. Dai, X. Shen, et al., Nitrogen-doped carbon dots anchored NiO/Co_3O_4 ultrathin nanosheets as advanced cathodes for hybrid supercapacitors, J. Colloid Interface Sci. 579 (2020) 282–289.
[28] N. Wang, Q. Liu, D. Kang, J. Gu, W. Zhang, D. Zhang, Facile self-cross-linking synthesis of 3D nanoporous Co_3O_4/carbon hybrid electrode materials for supercapacitors, ACS Appl. Mater. Interfaces 8 (25) (2016) 16035–16044.
[29] D. Kong, C. Cheng, Y. Wang, B. Liu, Z. Huang, H.Y. Yang, Seed-assisted growth of α-Fe_2O_3 nanorod arrays on reduced graphene oxide: a superior anode for high-performance Li-ion and Na-ion batteries, J. Mater. Chem. A 4 (30) (2016) 11800–11811.
[30] Z. Li, J. Han, L. Fan, R. Guo, In-situ controllable growth of α-$Ni(OH)_2$ with different morphologies on reduced graphene oxide sheets and capacitive performance for supercapacitors, Colloid Polym. Sci. 294 (4) (2016) 681–689.
[31] J. Gu, L. Sun, Y. Zhang, Q. Zhang, X. Li, H. Si, et al., MOF-derived Ni-doped CoP@C grown on CNTs for high-performance supercapacitors, Chem. Eng. J. 385 (2020) 123454.
[32] Y.-C. Chung, A. Julistian, L. Saravanan, P.-R. Chen, B.-C. Xu, P.-J. Xie, et al., Hydrothermal synthesis of CuO/RuO_2/MWCNT nanocomposites with morphological variants for high efficient supercapacitors, Catalysts 12 (1) (2021) 23.
[33] S. Kumar, G. Saeed, L. Zhu, K.N. Hui, N.H. Kim, J.H. Lee, 0D to 3D carbon-based networks combined with pseudocapacitive electrode material for high energy density supercapacitor: a review, Chem. Eng. J. (2021) 403.
[34] E. Dhandapani, S. Thangarasu, S. Ramesh, K. Ramesh, R. Vasudevan, N. Duraisamy, Recent development and prospective of carbonaceous material,

conducting polymer and their composite electrode materials for supercapacitor — a review, J. Energy Storage 52 (2022).
[35] Y. Zhao, A. Wang, L. Shen, L. Xiao, L. Hou, Carbohydrate assisted preparation of N-doped hierarchically porous carbons from melamine resin via high internal phase emulsion template, Microporous Mesoporous Mater. 341 (2022).
[36] A. Rashti, B. Wang, E. Hassani, F. Feyzbar-Khalkhali-Nejad, X. Zhang, T.-S. Oh, Electrophoretic deposition of nickel cobaltite/polyaniline/rGO composite electrode for high-performance all-solid-state asymmetric supercapacitors, Energy Fuels 34 (5) (2020) 6448–6461.
[37] X. Wu, F. Zeng, X. Song, X. Sha, H. Zhou, X. Zhang, et al., In-situ growth of Ni(OH)2 nanoplates on highly oxidized graphene for all-solid-state flexible supercapacitors, Chem. Eng. J. 456 (2023).
[38] Y. Xin, X. Dai, G. Lv, X. Wei, S. Li, Z. Li, et al., Stability-enhanced α-$Ni(OH)_2$ pillared by metaborate anions for pseudocapacitors, ACS Appl. Mater. Interfaces 13 (24) (2021) 28118–28128.
[39] A.S. Najm, H.S. Naeem, H.S. Majdi, S.A. Hasbullah, H.A. Hasan, K. Sopian, et al., An in-depth analysis of nucleation and growth mechanism of CdS thin film synthesized by chemical bath deposition (CBD) technique, Sci. Rep. 12 (1) (2022) 15295.
[40] A. Fatemi, T. Tohidi, K. Jamshidi-Galeh, M. Rasouli, K. Ostrikov, Retraction Note: optical and structural properties of Sn and Ag-doped PbS/PVA nanocomposites synthesized by chemical bath deposition, Sci. Rep. 14 (1) (2024) 3708.
[41] Y. Zhao, Z. Zhao, Z. Zhu, A. Wang, L. Hou, Preparation of N-doped porous carbons via high internal phase emulsion template, Prog. Nat. Sci. Mater. Int. 31 (2) (2021) 270–278.
[42] J. Xie, P. Yang, Y. Wang, T. Qi, Y. Lei, C.M. Li, Puzzles and confusions in supercapacitor and battery: theory and solutions, J. Power Sources 401 (2018) 213–223.
[43] Y. Zhao, H. Chen, L. Xiao, X. Yin, L. Hou, Oxygen-enriched hierarchical porous carbon supported Co-Ni nanoparticles for promising hybrid supercapacitors via one step pyrolysis of polymerized high internal phase emulsion, J. Alloys Compd. 907 (2022) 164481.
[44] T. Zhang, R.A. Sanguramath, S. Israel, M.S. Silverstein, Emulsion templating: porous polymers and beyond, Macromolecules 52 (15) (2019) 5445–5479.
[45] L. Feng, M. Wang, Y. Chang, H. Song, W. Hou, Y. Zhang, et al., Polymerization-pyrolysis-derived hierarchical nitrogen-doped porous carbon for energetic capacitive energy storage, ACS Appl. Energy Mater. 6 (13) (2023) 7147–7155.
[46] C. Song, H. Lin, T. Wang, B. Li, R. Lu, S. Zhang, Targeted synthesis of "urechis unicinctus"-like nitrogen-doped porous carbon nanorods for supercapacitors, Energy Fuels 37 (10) (2023) 7511–7521.
[47] M. Wang, H. Liu, D.D. Zhai, X.Y. Chen, Z.J. Zhang, In-situ synthesis of highly nitrogen, sulfur co-doped carbon nanosheets from melamine-formaldehyde-thiourea resin with improved cycling stability and energy density for supercapacitors, J. Power Sources 416 (2019) 79–88.
[48] Y. Yang, X. Wang, F. Huang, J. Zhao, X. Wang, $Ni(OH)_2$ nanodot-decorated Co–Co LDH/C hollow nanocages for a high performance supercapacitor, Dalton Trans. 49 (47) (2020) 17310–17320.
[49] X. Zhang, B. Sun, X. Fan, P. Liang, G. Zhao, B.K. Saikia, et al., Hierarchical porous carbon derived from coal and biomass for high performance supercapacitors, Fuel 311 (2022) 122552.
[50] H.-S. Kim, J.B. Cook, H. Lin, Jesse S. Ko, H. Tolbert Sarah, V. Ozolins, et al., Oxygen vacancies enhance pseudocapacitive charge storage properties of MoO_{3-x}, Nat. Mater. 16 (4) (2017) 454–460.
[51] W. Niu, Z. Xiao, S. Wang, S. Zhai, L. Qin, Z. Zhao, et al., Synthesis of nickel sulfide-supported on porous carbon from a natural seaweed-derived polysaccharide for high-performance supercapacitors, J. Alloys Compd. 853 (2021) 157123.
[52] X. Pu, D. Zhao, C. Fu, Z. Chen, S. Cao, C. Wang, et al., Understanding and calibration of charge storage mechanism in cyclic voltammetry curves, Angew. Chem. Int. Ed. 60 (39) (2021) 21310–21318.
[53] N. Wang, Y. Yao, L. He, Y. Chen, B. Sun, One-step carbonization of poly(styrene/divinylbenzene) to fabricate N-doped porous carbon for high-performance supercapacitor electrode, J. Porous Mater. 27 (2) (2020) 627–635.
[54] Z. Shi, X. Xu, P. Jing, B. Liu, J. Zhang, Hierarchical nickel-cobalt hydroxide composite nanosheets-incorporated nitrogen-doped carbon nanotubes embedded with nickel-cobalt alloy nanoparticles for driving a 2 V asymmetric supercapacitor, ACS Appl. Mater. Interfaces 15 (5) (2023) 7263–7273.
[55] K. Zheng, L. Liao, Y. Zhang, H. Tan, J. Liu, C. Li, et al., Hierarchical NiCo-LDH core/shell homostructural electrodes with MOF-derived shell for electrochemical energy storage, J. Colloid Interface Sci. 619 (2022) 75–83.
[56] S. Li, Y. Luo, C. Wang, M. Wu, Y. Xue, J. Yang, et al., A novel hierarchical core-shell structure of NiCo2O4@NiCo-LDH nanoarrays for higher-performance flexible all-solid-state supercapacitor electrode materials, J. Alloys Compd. (2022) 920.
[57] Z. Li, Y. Huang, Z. Zhang, J. Wang, X. Han, G. Zhang, et al., Hollow C-LDH/Co(9)S (8) nanocages derived from ZIF-67-C for high- performance asymmetric supercapacitors, J. Colloid Interface Sci. 604 (2021) 340–349.
[58] T. Zhao, C. Liu, T. Meng, W. Deng, L. Zheng, F. Yi, et al., Graphene quantum dots pinned on nanosheets-assembled NiCo-LDH hollow micro-tunnels: toward high-performance pouch-type supercapacitor via the regulated electron localization, Small 18 (20) (2022) e2201286.
[59] W. Wang, N. Zhang, Z. Ye, Z. Hong, M. Zhi, Synthesis of 3D hierarchical porous Ni–Co layered double hydroxide/N-doped reduced graphene oxide composites for supercapacitor electrodes, Inorg. Chem. Front. 6 (2) (2019) 407–416.
[60] K. Le, Z. Wang, F. Wang, Q. Wang, Q. Shao, V. Murugadoss, et al., Sandwich-like NiCo layered double hydroxide/reduced graphene oxide nanocomposite cathodes for high energy density asymmetric supercapacitors, Dalton Trans. 48 (16) (2019) 5193–5202.
[61] H. Niu, Y. Zhang, Y. Liu, N. Xin, W. Shi, NiCo-layered double-hydroxide and carbon nanosheets microarray derived from MOFs for high performance hybrid supercapacitors, J. Colloid Interface Sci. 539 (2019) 545–552.